1 **Physical mechanisms for biological carbon uptake during the onset of the spring**

2 **phytoplankton bloom in the northwestern Mediterranean Sea (BOUSSOLE site)**

3 Liliane Merlivat[1], Michael Hemming [2], Jacqueline Boutin[1], David Antoine[3, 4], Vincenzo

4 Vellucci[5], Melek Golbol[5], Gareth A. Lee[6], Laurence Beaumont[7]

5 [1] Sorbonne Université, CNRS/IRD/MNHN, LOCEAN, IPSL, Paris, France

6 [2] Coastal and Regional Oceanography Lab, Centre for Marine Science and Innovation, UNSW

7 Sydney, Sydney, NSW 2052 Australia

8 [3] Remote Sensing and Satellite Research Group, School of Earth and Planetary Sciences,

9 Curtin University, Perth, WA 6845, Australia

10 [4] Sorbonne Université, CNRS, Laboratoire d'Océanographie de Villefranche, Villefranche sur

11 Mer 06230, France

12 [5] Sorbonne Université, CNRS, Institut de la Mer de Villefranche, Villefranche sur Mer 06230,

13 France

14 [6] Centre for Ocean and Atmospheric Sciences, School of Environmental Sciences, University

15 of East Anglia, Norwich Research Park, Norwich NR4 7TJ, UK

16 [7] Division Technique INSU-CNRS, 92195 Meudon CEDEX, France

18 Correspondence to: liliane.merlivat@gmail.com

19 Keywords: Bloom onset ; Carbon uptake ; Air-sea interaction; Mediterranean sea

20 Abstract

21 Several trigger mechanisms have been proposed for the onset of the phytoplankton spring

22 bloom. Among these, that phytoplankton cells begin to bloom when they experience higher

23 average light levels in shallower mixed layers, a result of the surface net heat fluxes becoming

24 positive and wind strength decreasing. We study the impact of these two forcings in the

25 northwestern Mediterranean Sea. We take advantage of hourly measurements of oceanic and

26 atmospheric parameters collected at two neighboring moorings during the months of March

27 and April in the years 2016 to 2019, combined with glider data in 2016. The onset of the

surface phytoplankton growth is concomitant with the start of significant biological activity detected by a sudden decrease in dissolved inorganic concentrations derived from measurements in the upper 10 m of the water column. A rapid reduction in wind stress following high-wind events is observed at the same time. A resulting shallow mixing layer favors carbon uptake by phytoplankton lasting a few days. Simultaneously, the air-sea net heat flux switches from negative to positive linked to changes of the latent air-sea heat flux, which is proportional to the wind speed. This results in an increased thermal stratification of the ocean's surface layers. In 2016, glider data show that the mixing layer is significantly shallower than the mixed layer at the onset of the surface phytoplankton bloom. We conclude that decreases in the mixing and mixed layer depths lead to the onset of the phytoplankton bloom due to the relaxation of wind speed following storms. We estimate net daily community production in the mixing layer over periods of 3 days between 2016 and 2019 as between 38 mmol C m$^{-2}$ and 191 mmol C m$^{-2}$. These results have important implications as biological processes play a major role in the seasonal evolution of surface pCO2 and thereby the rate of reduction of atmospheric $CO_2$ by exchange at the air-sea interface.

Introduction

Investigating the physical and biological mechanisms contributing to changes in air-sea carbon dioxide ($CO_2$) fluxes is essential. It is a critical component of the global carbon cycle and the climate system with the ocean removing about a quarter of the $CO_2$ emitted into the atmosphere by human activities over the last decade. It depends on the gradient of $CO_2$ partial pressure, $pCO_2$, between the atmosphere and the surface ocean [Takahashi et al., 2009; Rödenbeck et al., 2013; Merlivat et al., 2015]. $pCO_2$ in the ocean mixed surface layer depends on the relative contribution of dynamic transport, thermodynamics and biogeochemistry. As the biological carbon pump lowers $pCO_2$ and Dissolved Inorganic Carbon (DIC) at the sea surface, the production of plankton biomass during a bloom can be sufficient to reverse the annual cycle of surface-ocean $CO_2$ uptake. A decrease in surface DIC, after physical processes have been eliminated, indicates the beginning of phytoplankton spring growth. Conceptual frameworks have been proposed to explain when depth-integrated

59   phytoplankton biomass starts accumulating during blooms [Behrenfeld, 2010; Sverdrup,
60   1953]. The timing of the initiation of the surface spring phytoplankton bloom depends in
61   particular on atmospheric forcing. The physical processes of wind stress, heat flux and
62   vertical mixing control the depth of the mixed/mixing layer and thus the availability of light
63   [Siegel et al, 2002, Chiswell, 2011; Taylor and Ferrari, 2011; Brody and Lozier, 2015;
64   Enriquez and Taylor, 2015, Rumyantseva et al, 2019].   Thus, to better understand which
65   fundamental physical processes control the timing of the onset of the surface bloom, in situ
66   measurements are needed at the appropriate hourly to daily timescale. It is important to draw
67   attention to the atmospheric forcing timescale. In biogeochemical ocean modeling studies,
68   typically built on atmospheric models, reanalysis or satellite data, time resolution of at best a
69   few days are required [Mahadevan et al, 2012].
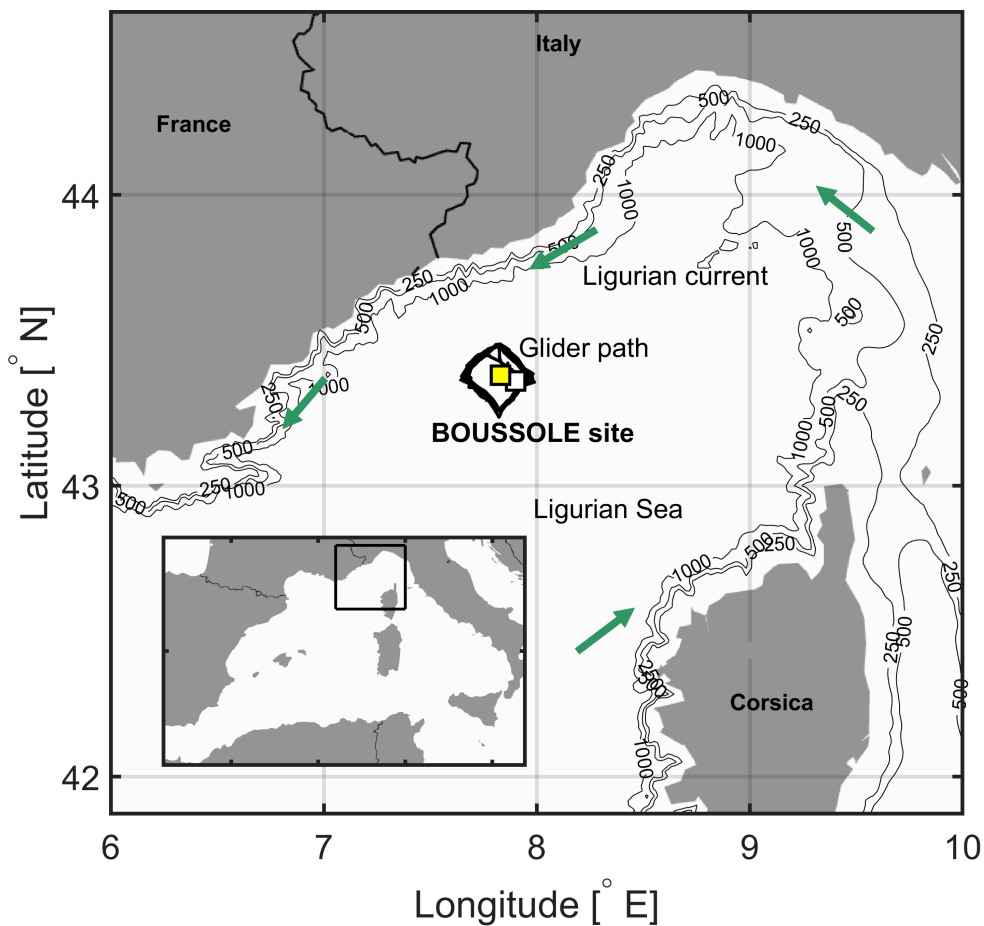
70

71   Figure 1. The area of the northwestern Mediterranean Sea showing the French and Italian
72   Rivieras, the island of Corsica, the main current branches (green arrows) in the Ligurian Sea
73   and the location of the BOUSSOLE buoy (white square) and the AZUR meteorological buoy
74   (yellow square). The black line indicates the glider's path in March-April 2016.

In the northwestern Mediterranean Sea, the BOUSSOLE (Bouée pour l'acquisition de Séries Optiques à Long Terme; Antoine et al., 2006, 2008a,b) buoy is located in the central area of the Liguro-Provençal basin (Fig.1), where the dominant ocean currents are generally weak (<20 cm s$^{-1}$) [Millot, 1999; Antoine et al., 2008b; Niewiadomska et al., 2008]. The main processes that govern the pCO$_2$ variations at the sea surface on an annual scale, after removal of the temperature effect, are vertical convective mixing and biological production [Begovic and Copin-Montégut, 2002; Copin-Montégut al., 2004; Hood and Merlivat, 2001; Merlivat et al., 2018]. Intense convection resulting from repeated high wind events in winter or early spring when atmospheric temperatures are typically low brings nutrients to the surface layer [Andersen and Prieur, 2000; Antoine et al., 2008b; Marty et al., 2002; Pasqueron de Fommervault et al., 2015].

The objective of this study is to examine the impact of atmospheric forcing on surface phytoplankton bloom initiation in the northwestern Mediterranean Sea. To this aim we use concurrent hourly data of seawater carbon chemistry measured at depths less or equal to 10 m at the BOUSSOLE mooring [Merlivat et al, 2018] and atmospheric flux measurements at the Azur meteorological buoy 3.1 nm (5.8 km) away from BOUSSOLE in March and April 2016 to 2019. Additional measurements of phytoplankton chlorophyll-a (Chla), temperature and density were provided by an underwater glider deployed in March-April 2016. The initiation of biological carbon uptake is revealed by the sudden decrease in DIC measured at the BOUSSOLE buoy.

In the Material and Methods section, we provide the description of data processing, theoretical framework, and calculations used to evaluate mixing regimes in the water column and net community production. The results section presents measured atmospheric and biogeochemical parameters observed in March-April, and NCP estimates from 2016 to 2019. The Discussion section relates our results to previous findings and presents our conclusions regarding the drivers of phytoplankton bloom initiation.

2 Material and methods

2.1- Data from the BOUSSOLE mooring

CARIOCA sensors [Merlivat and Brault, 1995] installed on the BOUSSOLE buoy (43°22'N, 7°54'E; Fig.1) monitored hourly partial pressure, pCO$_2$, at both 3 and 10 m alongside salinity

106 and temperature (SEABIRD Scientific SBE 37 MicroCAT CTDs). Protocols for calibration of

107 in situ measurements are described in [Merlivat et al, 2018]. CARIOCA measurements of

108 $pCO_2$ and temperature are combined with total alkalinity (Alk) derived from salinity

109 [Merlivat et al., 2018] to calculate DIC. The dissociation constants of Mehrbach et al., (1973)

110 refitted by Dickson and Millero (1987) are used, as recommended by Alvarez et al. (2014) for

111 the Mediterranean Sea. For the March-April months mean salinity is 38.3, corresponding with

112 mean Alk equal to 2571.4 $\mu$mol kg$^{-1}$ [Copin et al, 2004]. The expected precision of the

113 CARIOCA $pCO_2$, and DIC is 5 $\mu$atm, and 3 $\mu$mol kg$^{-1}$, respectively [Merlivat et al, 2018].

114 2.2- Glider observations

115 An iRobot Seaglider model 1KA (SG537) with an ogive fairing operated by the University of

116 East Anglia (UEA) [see Hemming et al., 2017] was deployed during the BOUSSOLE

117 monthly cruise (#169) [Golbol et al 2000] and recovered 1 month later with a ship of

118 opportunity. Diving to 1000 m, 147 dives were completed between March 7 and April 5 2016

119 repeatedly-sampling a square-shaped path surrounding the BOUSSOLE buoy (Fig. 1) with

120 corners pointing to cardinal directions. Out of 147 dives, a number of them contain data that

121 are within 10 km of the BOUSSOLE mooring, i.e. when it was sampling in the eastern corner

122 of the diamond path. The glider was equipped with a non-pumped SEABIRD Scientific SBE

123 9 CTD instrument package providing temperature and salinity, and a WET Labs Eco Puck

124 sensor providing relative phytoplankton Chla fluorescence, factory calibrated into Chla

125 concentration units (mg m$^{-3}$).

126 2.3- Azur meteorological buoy

127 The Azur meteorological buoy has been deployed since 1999 by the French weather forecast

128 Agency (Meteo-France) at 43°23'N, 7°50'E (Fig. 1). It provides hourly measurements of

129 surface wind speed extrapolated to 10 m height, $U_{10}$ (m s$^{-1}$), net incoming and emitted long-

130 wave radiation, incoming short-wave radiation, and the sensible and latent heat fluxes. These

131 are needed to estimate the net air-sea heat budget at the sea surface (http://mistrals.sedoo.fr).

132 $U_{10}$ is used to calculate wind stress, $\tau$, as follows: $\tau = \rho_a\, C_d\, U_{10}^2$, where $\rho_a$ is air density (1.2

133 kg m$^{-3}$), and $C_d$ is the drag coefficient (1.4 x 10$^{-3}$). Photosynthetically Active Radiation (PAR,

134 mol photons m$^{-2}$ d$^{-1}$) is related to solar irradiance (i.e. short-wave flux), SW, following PAR =

135 0.473 SW [Papaioannou et al., 1993].

136 2.4- Estimation of mixed and mixing layer depths

137  The mixing layer depth, $Z_{mx}$, is the upper part of a mixed layer of uniform density where

138  active turbulence occurs [Brainerd and Gregg 1995]. Several recent studies have highlighted

139  the significance of this layer to understand the phytoplankton phenology of phytoplankton

140  blooms [Brody and Lozier, 2015; Taylor and Ferrari, 2011]. Autonomous profiling floats

141  equipped with bio-optical sensors have also highlighted the importance of mixing rather than

142  mixed layers to characterize the onset and the development of a phytoplankton bloom. Wind-

143  driven and buoyancy-driven regimes control the characteristics and depth of active mixing

144  [Brody and Lozier, 2014, 2015, Ramuyantseva et al, 2015, Lacour et al, 2019, Pellichero et al,

145  2020]. Wind-driven mixing dominates in the presence of weak buoyancy forcing when heat

146  fluxes are small. In that case, the dominant mixing length scale is equal to the Ekman length

147  layer depth scale.

148  The daily mean mixed layer depth, $Z_{ml}$ is derived for 2016 from glider vertical profiles of

149  temperature and salinity using the algorithm provided by Holte and Talley, (2009) estimated

150  using the potential density algorithm.

151  To estimate $Z_{mx}$, $\tau$ is used to calculate the Ekman layer depth, $Z_{ek}$, $Z_{ek}=\gamma\, u_*/f$, where $\gamma$ is an

152  empirical constant (0.5), f is the Coriolis parameter ($10^{-4}$ s$^{-1}$) over the BOUSSOLE area, and

153  $u_*$ is the turbulent friction velocity, $u_* = \sqrt{\dfrac{\tau}{\rho_w}}$ (m s$^{-1}$), with $\rho_w$ the density of the surface sea

154  water [Lacour et al, 2019]. When heat fluxes are large and positive, Enrikez and Taylor

155  (2015) proposed to express the mixing depth $Z_{mx}$ in terms of the surface forcing, i.e. the

156  surface stress and a stabilizing surface buoyancy flux $B_0$, as follows:

157  $$\frac{1}{Z_{mx}^2} = \frac{f^2}{(C_3\, u_*)^2} + \frac{f\, B_0}{(C_4\, u_*^2)^2} \qquad (1)$$

158  With $C_3 = 1$, $C_4 = 0.57$, $B_0 = Q\,\lambda\, g\,/c_p\,\rho_0$, where Q is the net surface heat flux, $\lambda$ the thermal

159  expansion coefficient (1.65 $10^{-4}$ °C$^{-1}$), g the gravitational acceleration (9.81 m s$^{-2}$), $c_p$ the

160  specific heat of water (4 $10^{-3}$ J kg$^{-1}$ °C$^{-1}$) and $\rho_0$ the pure water density (1000 kg m$^{-3}$).

161  2.5-Estimation of euphotic zone depth

162  The euphotic depth, $Z_{eu}$, is generally derived as the depth where PAR is 1% of its surface

163  value. $Z_{eu}$ can be estimated from Chla at the surface using the method described by Lee et al.

164  (2007) based on the equation of Morel and Berthon (1989):

165  $$Z_{eu} = 34\,(Chla)^{-0.39} \qquad (2)$$

For the period between 2017 and 2019, GlobColour merged Chla products were used, which are based on satellite observations with a resolution of 25 km, and a binning period of 8 days (http://www.oceancolour.org). For 2016, glider surface Chla was used to derive Zeu instead of satellite measurements. We excluded glider Chla between 05:00 and 20:00 UTC affected by sunlight–induced fluorescence quenching, and we applied a depth-constant offset to glider measurements using Chla water samples available on March 7.

2.6-Estimation of average mixing layer irradiance

We calculate the average mixing layer irradiance, I, function of the incident surface irradiance, PAR, mixing layer depth, h, and the diffuse attenuation coefficient, $K_d$, estimated from surface chlorophyll-a concentrations (Venables and Moore, 2010 ).

$$K_d = 0.05 + 0.057 \, Chla^{0.58}$$

$$I = \frac{PAR}{K_d h} (1 - e^{-K_d h}) \quad (3)$$

2.7 – Estimation of net community production

Biological Net Community Production rates, NCP (mmol m$^{-2}$ day$^{-1}$), are calculated for separate 3-day periods in March-April, 2016 to 2019 from DIC concentrations derived from CARIOCA measurements, assuming that measurements in the top 10 m of the water column are representative of an homogeneous mixing layer [Boutin and Merlivat, 2009; Merlivat et al, 2015; Pelicherro et al, 2020]. In the study area, current velocities are expected to be small [Millot, 1999; Antoine et al., 2008; Niewiadomska et al., 2008], hence to estimate NCP, we ascertain that the contribution of horizontal advection was negligible. Vertical mixing events are identified by an increase in DIC resulting from upward movement of high DIC Levantine Intermediate Water (LIW) at approximately 200 m depth [Copin-Montégut and Bégovic, 2002]. We isolated time periods when local physical processes were largely one-dimensional in order to study changes in biological and chemical parameters that occurred during rapid transitions from deep mixing to intermittent stratification. In 2016, over a four-day period, March 18-21, the diurnal cycle of DIC values characterized by a maximum in the morning followed by a minimum at the end of the day indicates the onset of organic matter formation. The eddy diffusion term is negligible as the DIC gradient at the base of the mixing layer is very weak, entrainment is not expected as changes in DIC are observed during periods of

195 stratification. For the identified periods, biological production and air-sea exchange are the
196 dominant processes responsible for daily changes in DIC.

197 NCP is thus estimated from temporal variation of the DIC integrated over $Z_{mx}$ ($DIC_{int}$), and
198 corrected for the air-sea $CO_2$ flux contribution [Pelicherro et al, 2020]:

199 $$NCP = \left(\frac{\Delta DIC_{int}}{\Delta t}\right)_{bio} = \left(\frac{\Delta DIC_{int}}{\Delta t}\right)_{meas} - k \times s \times (pCO_{2atm} - pCO_{2sw}) \quad (4)$$

200 The first term in equation 4, $\left(\frac{\Delta DIC_{int}}{\Delta t}\right)_{meas}$, is the daily variation of $DIC_{int}$ calculated over 3
201 days from the date identified as the start of phytoplankton bloom ($t_0$), whilst the remaining
202 part corresponds to DIC variability due to air-sea $CO_2$ exchange, where k is the gas transfer
203 velocity [Wanninkhof, 2014], s is the solubility of $CO_2$ in seawater [Weiss, 1974], and
204 $pCO_{2sw}$ and $pCO_{2atm}$ are respectively the partial pressures of $CO_2$, in µatm, in sea water and in
205 air [Merlivat et al, 2018].

206 3 Results

207 3.1- Description of the 2016 time-series
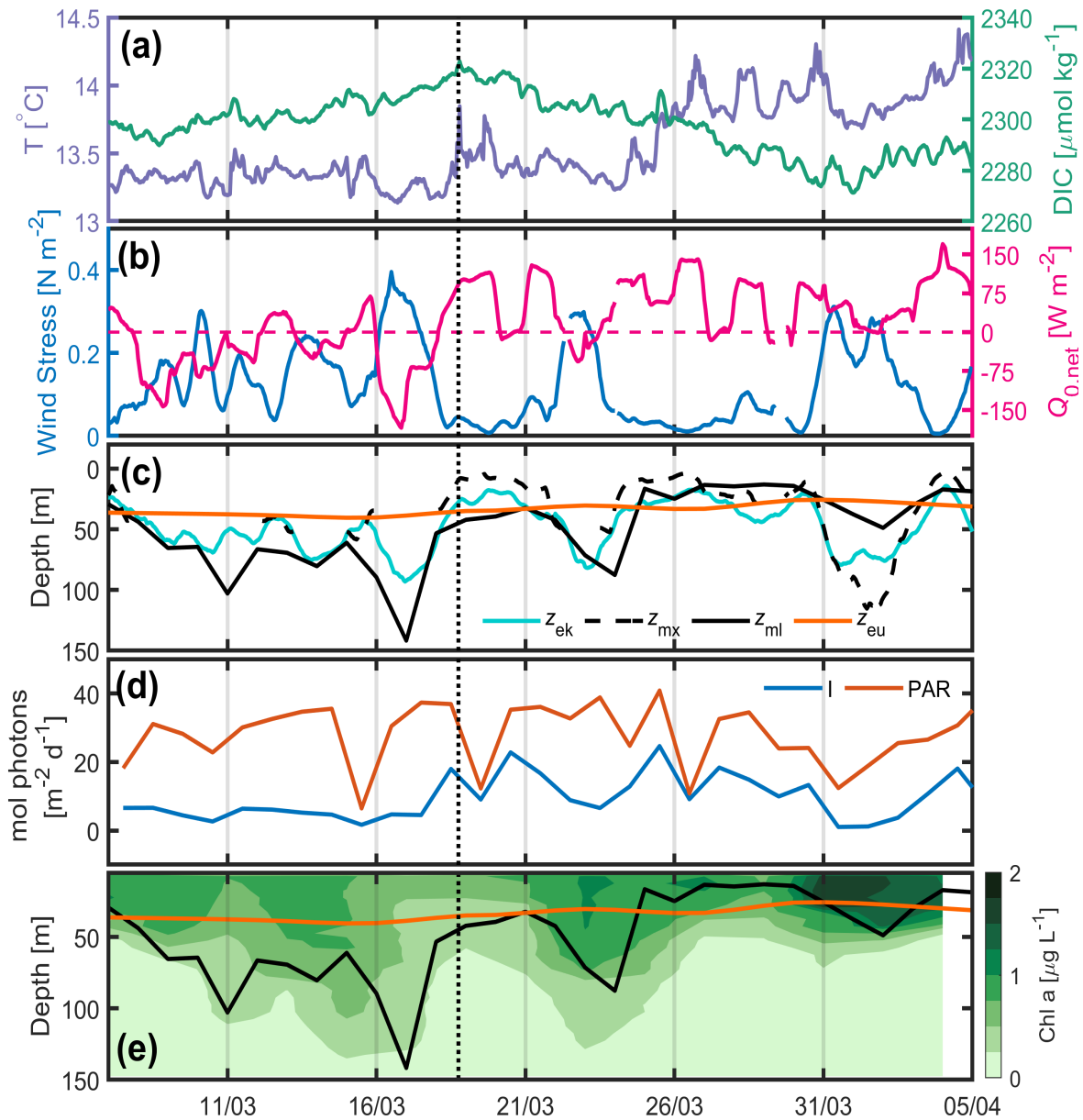
208

Figure 2. 2016 (a) Hourly DIC (green) and SST(purple) at the BOUSSOLE site, (b) hourly wind stress (blue) and net heat flux (pink) at the Azur buoy site. The pink dotted line indicates the change of sign of the net heat flux from negative to positive values, (c) daily depths of the mixed layer (black), mixing layer (dotted black), Ekman layer (cyan) and euphotic layer (orange) at the BOUSSOLE site. The black dotted line on panels (a), (b), (c) (d) and (e) indicates the onset time of the bloom (March 18). (d) PAR (orange) and I, average mixing layer irradiance (blue), (e) Glider-derived depths of the mixed layer (black curve, same as in (c)), euphotic layer (orange), and nighttime 2-day binned chlorophyll concentration (green coloring) retrieved between March 7 and April 5.

The temporal evolution of physical and biogeochemical parameters between March 7 and April 5 2016 is displayed in Fig. 2. It shows an initial increase in DIC until March 18 (Fig. 2a), resulting from the vertical mixing of surface waters with the DIC-enriched underlying LIW [Copin-Montégut and Bégovic, 2002], followed by a decrease in DIC that corresponds to an increase of surface Chla (Fig 2e). Temperature increases intermittently over the same time period (Fig. 2a), with a sharp increase on March 18 and 25. Before March 18 frequent atmospheric fronts associated with wind forcing between 0.2 and 0.5 N m$^{-2}$ were observed (Fig. 2b). $Q_{0,net}$ was negative most of the time leading up to March 18, but mostly positive afterwards (Fig. 2b). A clear anticorrelation was observed between $\tau$ and $Q_{0,net}$ (Fig. 2b). The mixed-layer depth derived from the glider measurements (< 20 km away from the Boussole site) deepened to > 70 m at times between March 8 and March 18, consistent with the passage of frequent atmospheric fronts. From March 18 to April 5, $Z_{ml}$ shoaled from ~ 45 m to ~10 m, excluding two short periods around March 24 and April 2 when atmospheric fronts were passing (Fig. 2c). From March 18 to 31, $Z_{mx}$ was for a considerable time either shallower than, or at similar depth to $Z_{ml}$ and $Z_{eu}$ (Fig. 2c). The start of the increase in PAR from March 15 precedes the increase in irradiance by 3 days as a result of the decrease of the mixing layer depth observed only after March 18 (Fig. 2d**).**

From March 18 to April 5, an increase in glider Chla was observed in the upper layer (Fig. 2e) as the result of the biomass accumulation within the water column following the initial growth of surface phytoplankton [Behrenfeld, M. and E. Boss, 2014]. The same was observed in the Southern Ocean [Pelicherro et al, 2019].

3.2- Description of the 2017-2018-2019 time-series

Only measurements at the BOUSSOLE and Azur buoys were available between 2017 and 2019. Here we focus on the periods between March 1 and April 25. In 2017, from March 9, after the passage of a very active atmospheric front ($\tau$ up to 2.7 N m$^{-2}$), a decrease in DIC accompanied by an increase in temperature was observed for a period of 14 days despite a few short bursts of vertical mixing, typically lasting less than 1 day (Fig.3a, d, g). At the same time, the net surface heat flux switched from negative to positive most of the time. Over this 14-day period, $Z_{mx}$ was predominantly shallower than the $Z_{eu}$ at times when DIC was decreasing.

In 2018 (Fig. 3b, e, h) and 2019 (Fig. 3c, f, i), the weather records throughout the month of March are very similar, showing a succession of very strong wind events at the start of the

investigated time periods, with $\tau$ values of up to 3.7 N m$^{-2}$ and $Z_{ek}$ values as deep as 300 m. On April 5, 2018, following a period of high wind stress resulting in the formation of a deep mixing layer (~250 m), a decrease in DIC and an increase in SST were observed over 3 days. At the same time, the net heat flux oscillated around zero. In 2019, CARIOCA data were only available after March 24. On March 30, 3 days after high winds, a decrease in DIC and an increase in temperature lasted 3 days, while simultaneously the net heat flux reversed from negative to positive.
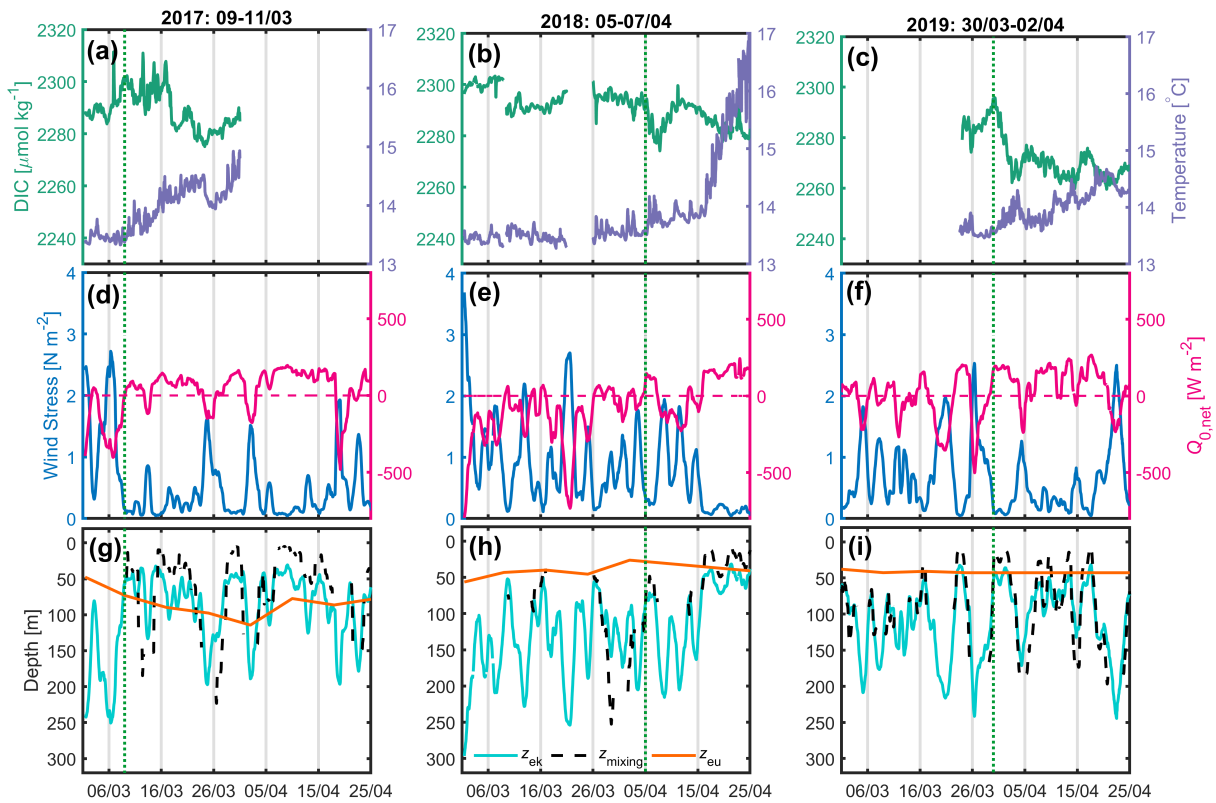
Figure 3. (a, b, c) 2017, 2018 and 2019 DIC (green) and SST (purple) at the BOUSSOLE site, (d, e, f) wind stress (blue) and net heat flux (red) at the Azur buoy site. (d, e, f) The red dotted line indicates the change of sign of the net heat flux from negative to positive values, (g, h, i) depths of the mixing layer (dotted black), Ekman layer (cyan) and euphotic layer (orange) at the BOUSSOLE site. The vertical dotted green line indicates the onset of the decrease of DIC.

For the period between 2017 and 2019, only satellite chlorophyll-a concentrations with a binning period of 8 days were available, which is too large to calculate the average mixing irradiance as it is highly variable on a daily scale (Fig 2.d).

267   3.3- NCP

268   NCP was estimated (Eq. 3) for 3-day periods over the four time-series between 2016 and
269   2019 (Table 1). Because we compute NCP only during periods when $Z_{ml}$ and $Z_{mx}$ shoal and
270   the air-sea $CO_2$ flux is very small, the measured total daily changes of DIC, dDIC/dt
271   (correlation coefficient, $r^{*2}$ >0.70), is expected to represent the biological consumption of
272   DIC. In 2016, 2017, and 2019, daily biological carbon uptake fluxes are between 38 and 191
273   mmol $m^{-2}$ $d^{-1}$. PAR and I vary respectively from 30 to 53 and 13 to 25 mol photons $m^{-2}$ $d^{-1}$ for
274   the four considered periods (Table 2).

| | $T_0$ | dDIC/dt [a] | $r^{*2}$ [b] | $\Delta DIC / \Delta t$ [c] | $r^{*2}$ [d] | air-sea flux $CO_2$ [e] | NCP [f] |
|---|---|---|---|---|---|---|---|
| | | µmol $kg^{-1}d^{-1}$ | | mmol $m^{-2}d^{-1}$ | | mmol $m^{-2}d^{-1}$ | mmol $m^{-2}$ $d^{-1}$ |
| **2016** 10m | March 18 | -3.0 | 0.80 | -37 | 0.68 | 1 | 38 |
| **2017** 3m | March 9 | -4.5 | 0.84 | -188 | 0.86 | 3 | 191 |
| **2018** 3m | April 5 | -6.5 | 0.70 | | | 17 | |
| **2019** 10m | March 30 | -8.3 | 0.93 | -163 | 0.63 | 4 | 167 |

275

276   Table 1. Net community production computed in the mixing layer over 3 days (NCP) after the
277   bloom onset ($T_0$). (a, b) variation of DIC at the measurement depth and linked correlation
278   coefficient; (c, d) change of integrated DIC over $Z_{mx}$ and linked correlation coefficient ;(e)
279   $CO_2$ flux from the atmosphere to the ocean; (f), absolute value of calculated NCP is
280   considered in order to provide positive values throughout the presentation and discussion in
281   the manuscript.

282

283   4 Discussion

284   4.1 Analysis of the physical drivers of the bloom initiation over the 4 years, 2016-2019

285   4.1.1 In 2016, the consumption of carbon indicated by the decrease in DIC from March 18
286   attests the initiation of the formation of phytoplankton biomass (Fig. 2,). Between 2

287  successive days, March 17 and 18, a rapid decrease in daily wind stress from 0.24 to 0.04 N

288  m$^{-2}$ results in a change of sign of the net heat flux from -68 to +56 W m$^{-2}$ (Fig.4a) and a

289  shoaling $Z_{mx}$, which is for the most part shallower than $Z_{eu}$ (Fig.4b) after March 18.

290
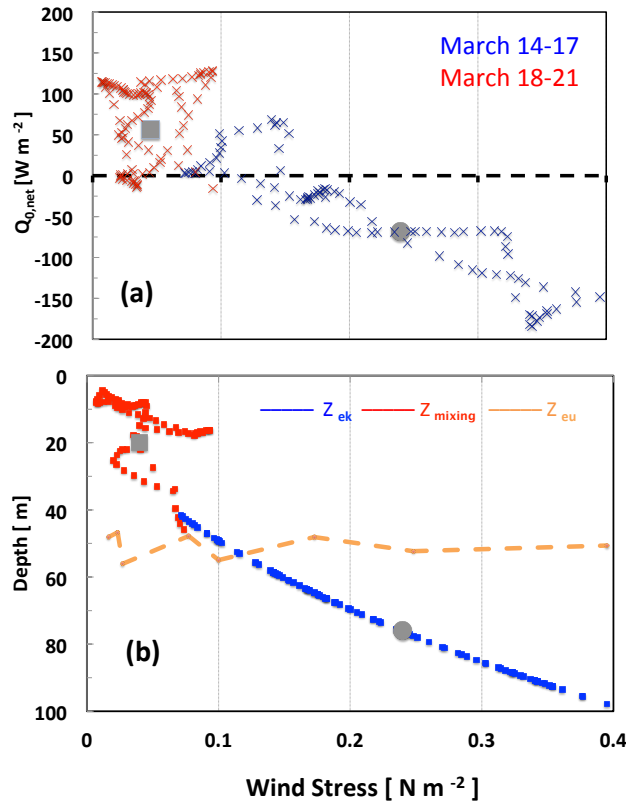
291  Figure 4. Changes of physical parameters (hourly values) at the onset of the 2016 bloom

292  during 2 consecutive periods of 4 days, March 14-17 (blue) and March 18-21 (red) as a

293  function of wind stress (a) net surface heat flux (b) depths of the Ekman, mixing and euphotic

294  layer. Grey circles and grey squares indicate mean values respectively on March 17 and

295  March 18. For comparison, the orange line shows the euphotic layer depth (March 14-21).

296  This illustrates the very fast change in heat flux and mixing layer thickness resulting from the

297  decrease in wind stress. The main drivers to explain the initiation of near surface spring

298  phytoplankton blooms proposed by  [Taylor and Ferrari, 2011, Brody-Lozier, 2014, 2015] are

299  a decrease in wind strength, a positive surface heat flux, and a decrease in the dominant

300  mixing length scale. Our results indicate that a decrease in $\tau$ is a common component for these

301  last two mechanisms (Fig.4). The variability of $Q_{0,net}$ is strongly controlled by the variability

302  of the latent heat flux proportional to the wind speed. From March 17 to 18, the latent heat

303  flux changed by 84 W m$^{-2}$ representing nearly 2 thirds of the total change of $Q_0$, with the
304  remainder originating from an increased short-wave flux. Hence, $Q_{0,net}$ increased as $\tau$
305  decreased. In the same way $Z_{mx}$, which is related to $\tau$ and $Q_{0,net}$, decreased. This highlights the
306  major contribution of wind stress relaxation in controlling the net surface heat flux, and
307  subsequent stratification leading to sallower $Z_{mx}$

308  4.1.2 Over the 4 years, 2016-2019, during the months of March and April, at the very
309  beginning of spring, the conditions required for initiating the spring bloom are very similar
310  although the range of wind stress values is smaller in 2016 (Fig. 2, Fig. 3). The wind stress
311  values are low following storm events. For all years except 2018, $Z_{mx}$ is smaller than $Z_{eu}$. The
312  average atmospheric and oceanographic conditions during the onset of the bloom are shown
313  in Table 2. The decrease of wind-driven mixing is then a dominant physical mechanism,
314  namely mixed layer shoaling which best predicts the timing of the spring bloom [Brody
315  Lozier, 2014, 2015]. Likewise, in the Southern Ocean, Pelicherro et al (2020) showed that a
316  bloom is initiated only when the wind-driven mixed layer decreases, even if the net heat flux
317  has been positive for some months.

318  4.2 DIC, Chla, Irradiance at the ocean surface in 2016

319  Between 18 and 21 March, a diurnal cycle in DIC is observed (Figure 5a) characterized by a
320  maximum in the morning followed by a minimum at the end of the day, indicating the onset
321  of organic matter formation. The decrease in DIC is accompanied by an increase of glider
322  surface Chla on 18 March and a simultaneous increase in the average mixing layer irradiance
323  (Fig. 5 b). It is worth noting that the Chla maximum does not occur until 31 March, 13 days
324  after the decrease in DIC. This maximum is the one identified in most cases by the Chla
325  satellite measurements with a binning period of 8 days. It follows that satellite data cannot
326  accurately characterize the conditions that prevail for the onset of a bloom, as these are
327  dictated by a great temporal variability of atmospheric forcings. Due to the seasonal
328  increase of surface irradiance in March-April, as well as the availability of nutrients following
329  vertical mixing with intermediate nutrient-enriched waters [Begovic and Copin-Montégut,
330  2002], the conditions for the onset of a bloom are met.

331

332
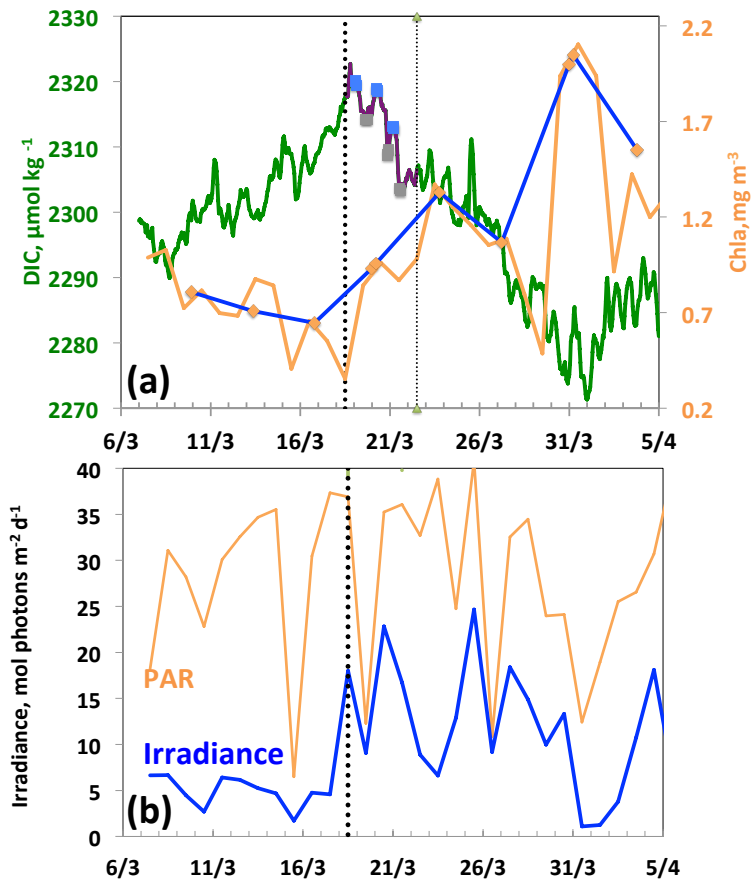
333

Figure 5. From March 7 to April 5, (a) DIC and Chla. The purple line and the squares
(blue,morning; grey, evening) indicate the 3 days biological diurnal DIC changes during the
period considered to compute NCP The blue and orange lines indicate the surface Chla when
the glider was at a distance of less than 5 km (blue) and less than 20 km (orange) respectively
from the Boussole buoy. (b) PAR and I average mixing layer irradiance. The vertical dotted
black line indicates the onset of the bloom on March 18.

4.3- Biological carbon uptake

In 2016, 2017, and 2019, at the onset of the bloom $Z_{mx}$ is shallower than $Z_{eu}$ (Table 2). Two
factors account for the observed large range of NCP variability at the time of triggering the
bloom: dDIC/dt and $Z_{ml}$. In 2016 and 2017, DIC decreased over a period of 14 days, whereas
it lasted for 3 days in 2018 and 2019, as a result of short-lived high wind events ($\tau > 1$ N m$^{-2}$).
On April 2, 2018, a high surface phytoplankton Chla, 1.9 mg m$^{-3}$, was measured by satellite
(Globcolour data) suggesting a strong biological signal. However, as $Z_{eu}$ is significantly
shallower than $Z_{mx}$ (26 m vs. 65m; Fig. 3h), it would be incorrect to estimate NCP integrated
over $Z_{mx}$ using the DIC gradient measured at 3 m depth and likewise to compute the average
mixing layer irradiance.

350 At the nearby DyFAMed site (Dynamique des Flux Atmospheriques en Mediterranee), using

351 a 20-year $O_2$ time series, Coppola et al. (2018) estimated an annual net community carbon

352 production equal to 7.1 mol m$^{-2}$ yr$^{-1}$, or 19.4 mmol m$^{-2}$ d$^{-1}$. Additionally, using

353 determinations of primary production from $^{14}$C in-situ incubations and of carbon export fluxes

354 from sediment traps at DyFAMed, Marty and Chiaverini (2002) calculated average daily

355 primary productions between 19.6 and 53 mmol m$^{-2}$ d$^{-1}$. These estimates may have

356 underestimated the annual NCP values as they were calculated from monthly observations

357 while phytoplankton production varies on a daily timescale. Our DIC measurements highlight

358 the large short-term variability of carbon consumption over a few days in March-April when

359 bloom-triggering atmospheric conditions are met, such as a seasonal light increase and the

360 availability of nutrients.

| | $T_0$ | Wind stress | Net heat flux | PAR | $Z_{mixing}$ | $Z_{Euphotic}$ | Irradiance |
|---|---|---|---|---|---|---|---|
| | | N m$^{-2}$ | W m$^{-2}$ | mol photons m$^{-2}$d$^{-1}$ | m | m | mol photons m$^{-2}$d$^{-1}$ |
| **2016** | March 18 | 0.04 +/0.02 | 56+/-36 | 37+/-3 | 20+/-9 | 47 | 18 |
| **2017** | March 9 | 0.12+/-0.02 | 45+/-21 | 30+/-3 | 28+/-12 | 71 | 13 |
| **2018** | April 5 | 0.30+/-0.24 | 127+/-12 | 42+/-6 | 62+/-9 | 29 | |
| **2019** | March 30 | 0.10+/-0.02 | 183+/-9 | 53+/-2 | 20+/-5 | 43 | 25 |

361

362 Table 2.  2016-2019.  Atmospheric drivers of the onset of the bloom: average values and

363 standard deviation on the day of the start of the bloom, $T_0$.

364

365 5- Concluding remarks

366 Around March and April in the northwestern Mediterranean Sea, the seasonal change in

367 lighting conditions and atmospheric forcing are the essential parameters that control the

368 triggering of near-surface phytoplankton blooms. These mechanisms have been highlighted

369 through the coupling of high-frequency physical and biogeochemical in situ observations. For

370 years 2016 to 2019, a bloom started in March or early April identified by a decrease in surface

371 DIC, following a period of intense mixing. The rapid decrease in surface wind speed entailed

372 a switch from negative to positive air-sea net heat fluxes, essentially due to changes in the

latent air-sea heat flux proportional to wind speed. These analysis support the hypothesis that decreases in the depth of active mixing, a result of the transition from buoyancy-driven to wind-driven mixing, control the timing of the surface spring bloom.

We have shown that the onset of surface phytoplankton growth, identified in 2016 by a simultaneous initial decrease in DIC and an increase in surface Chla, precedes by a few days the surface chlorophyll maximum as detected by satellite measurements with a binning period of 8 days. This time span does not allow to identify precisely the contribution of atmospheric drivers to trigger the onset of the growth of phytoplankton as it occurs on a daily basis.

Data availability

BOUSSOLE data (2016-2019) are available in the SEANOE data base (Merlivat Liliane, Boutin Jacqueline (2020). Mediterranean Sea surface $CO_2$ partial pressure and temperature data. SEANOE. https://doi.org/10.17882/56709

Azur Meteorological buoy: http://mistrals.sedoo.fr

SChl, 8-day, 4 km x4 km resolution, level 3 mapped ocean color product distributed by the European Space Agency, available at http://www.ocean colour/org

All glider data is archived at the British Oceanographic Data Centre (BODC, https://www.bodc.ac.uk/data/bodc_database/gliders/ ).

Author contributions: VV and MG were respectively in charge of the BOUSSOLE mooring buoy maintenance and monthly water sampling. LB was responsible for the laboratory preparation and calibration of the CARIOCA sensors. GAL led the UEA glider mission in March-April 2016. DA and VV provided data and funding through the BOUSSOLE project and contributed to writing and editing of the manuscript.

The authors declare that they have no conflict of interest.

Acknowledgments: Michael Hemming was a PhD student at the University of East Anglia and Sorbonne University under the supervision of Prof. Jan Kaiser, Prof. Karen J. Heywood, Dr Dorothee Bakker and Dr Jacqueline Boutin, funded by the Defence, Science and

401    Technology Laboratory (Contract no. DSTLX1000092277) with cooperation with Direction

402    Générale de l'Armement (DGA)-. The assistance of the UEA Glider Group in keeping the

403    glider flying is also gratefully acknowledged. The BOUSSOLE time series project is funded

404    by the Centre National d'Etudes Spatiales (CNES) and the European Space Agency

405    (ESA/ESRIN contract 4000119096/17/I-BG). The authors acknowledge Météo-France for

406    supplying the data from the Azur buoy and the HyMeX database teams (ESPRI/IPSL and

407    SEDOO/Observatoire Midi-Pyrénées) for their help in accessing their data. Crew and

408    Captains of R/V Tethys II are warmly thanked for assistance with operations at sea.

409

410    References

411    Álvarez, M., Sanleón-Bartolomé, H., Tanhua, T., Mintrop, L.,Luchetta, A., Cantoni, C.,

412    Schroeder, K., and Civitarese, G.: The CO2 system in the Mediterranean Sea: a basin wide

413    perspective, Ocean Sci., 10, 69–92, https://doi.org/10.5194/os-10-69-2014,2014.

414    Andersen, V. and Prieur, L.: One-month study in the open NW Mediterranean Sea

415    (DYNAPROC experiment, May 1995): Overview of hydrobiogeochemical structures and

416    effects of wind events, Deep-Sea Res. I, 47, 397–422, 2000.

417    Antoine, D. M. Chami, H. Claustre, F. D'Ortenzio, A. Morel, G. Bécu, B. Gentili, F. Louis ,J.

418    Ras, E. Roussier, A.J. Scott, D. Tailliez, S. B. Hooker, P. Guevel, J.-F. Desté, C. Dempsey

419    and D. Adams. 2006, BOUSSOLE : a joint CNRS-INSU, ESA, CNES and NASA Ocean

420    Color Calibration and Validation Activity. NASA Technical memorandum, N° TM-2006-

421    214147, NASA/GSFC, Greenbelt, USA.

422    Antoine, D., P. Guevel, J.-F. Desté, G. Bécu, F. Louis, A.J. Scott and P. Bardey: The

423    «BOUSSOLE» buoy; a new transparent-to-swell taut mooring dedicated to marine optics:

424    design, tests and performance at sea, Journal of Atmospheric and Oceanic Technology, 25,

425    968-989, 2008a.

426    Antoine, D., F. d'Ortenzio, S. B. Hooker, G. Bécu, B. Gentili, D. Tailliez, and A. J. Scott:

427    Assessment of uncertainty in the ocean reflectance determined by three satellite ocean color

428    sensors (MERIS, SeaWiFS and MODIS-A) at an offshore site in the Mediterranean Sea

429    (BOUSSOLE project), Journal of Geophysical Research, 113(C7), 2008b.

430    Begovic , M., and C. Copin-Montegut, Processes controlling annual variations in the partial

431    pressure of fCO2 in surface waters of the central northwestern Mediterranean sea (Dyfamed

432    site), Deep-Sea Research II, 49, 2031-2047, 2002

433    Behrenfeld, M. J, Abandoning Sverdrup's critical depth hypothesis on phytoplankton blooms.

434    Ecology, 91(4), 977-989, 2010

435    Behrenfeld, M. and E. Boss, Resurrecting the ecological underpinnings of ocean plankton

436    blooms. Annual Review of Marine Science, 6, 167-194, DOI: 10.1146/annurev-marine-

437    052913-021325, 2014

438    Brainerd, K. E., and Gregg, M. C, Surface mixed and mixing layer depths. Deep Sea Research

439    I: Oceanographic Research Papers, 42:1521–1543, 1995

440    Brody, S., and Lozier,M. Changes in dominant mixing length scale as a driver of

441    phytoplankton bloom initiation in the North Atlantic, Geophysical Research Letters 41, 3197–

442    3206, 2014.

443    Brody, S. R., & Lozier, M. S. , Characterizing upper-ocean mixing and its effect on the spring

444    phytoplankton bloom with in situ data. ICES Journal of Marine Science, 72(6), 1961-1970,

445    2015.

446    Chiswell, S. M.: Annual cycles and spring blooms in phytoplankton: don't abandon Sverdrup

447    completely. Marine Ecology Progress Series, 443, 39-50, 2011.

448    Copin-Montégut, C., Begovic, M.: Distributions of carbonate properties and oxygen along the

449    water column (0– 2000 m) in the central part of the NW Mediterranean Sea (Dyfamed site).

450    Influence of winter vertical mixing on air– sea CO2 and O2 exchanges. Deep-Sea Res., Part 2,

451    Top. Stud. Oceanogr. 49, 2049– 2066, 2002.

452    Copin-Montégut, C., M. Bégovic, and L. Merlivat.: Variability of the partial pressure of CO2

453    on diel to annual time scales in the Northwestern Mediterranean Sea, Mar Chem, 85(3-4),

454    169-189, 2004.

455    Coppola, L., Legendre, L., Lefevre, D., Prieur, L., Taillandier, V., & Riquier, E. D. :

456    Seasonal and inter–annual variations of dissolved oxygen in the northwestern Mediterranean

457    Sea (DYFAMED site). Progress in Oceanography, 2018.

458    Dickson, A. G., and F. J. Millero .: A comparison of the equilibrium constants for the

459    dissociation of carbonic acid in seawater media, Deep Sea Research Part A. Oceanographic

460    Research Papers, 34(10), 1733-1743 1987.

461    Enriquez, R.M., Taylor, J.R: Numerical simulations of the competition between wind-driven

462    mixing and surface heating in triggering spring phytoplankton blooms. ICES J. Mar. Sci. J. du

463    Cons. fsv071, 2015.

464    Golbol, M., Vellucci, V., Antoine, D .: BOUSSOLE, https://doi.org/10.18142/1, 2000.

465    Hemming, M. P., Kaiser, J., Heywood, K. J., Bakker, D. C., Boutin, J., Shitashima, K., Onken,

466    R. : Measuring pH variability using an experimental sensor on an underwater glider. Ocean

467    Science, 13 , 427–442,2017.

468    Holte, J., & Talley, L. : A new algorithm for finding mixed layer depths with applications to

469    Argo data and Subantarctic Mode Water formation. Journal of Atmospheric and Oceanic

470    Technology, 26(9), 1920-1939, 2009.

471    Hood, E. M., and L. Merlivat .: Annual and interannual variations of fCO2 in the

472    northwestern Mediterranean Sea: Results from hourly measurements made by CARIOCA

473    buoys, 1995-1997, J Mar Res, 59, 113-131, 2001.

474    Lacour, L., Briggs, N., Claustre, H., Ardyna, M., & Dall'Olmo, G.: The intraseasonal

475    dynamics of the mixed layer pump in the subpolar North Atlantic Ocean: A

476    Biogeochemical‐Argo float approach. Global Biogeochemical Cycles, 33(3), 266–281,2019.

477    Lee, Z., Weidemann, A., Kindle, J., Arnone, R., Carder, K. L., & Davis, C. : Euphotic

478    zone depth: Its derivation and implication to ocean-color remote sensing. Journal of

479    Geophysical Research: Oceans , 112 (C3),2007.

480    Mahadevan, A., D'asaro, E., Lee, C., & Perry, M. J. : Eddy-driven stratification initiates

481    North Atlantic spring phytoplankton blooms. Science, 337(6090), 54-58, 2012.

482    Marty, J.-C., Chiavérini, J. .: Seasonal and interannual variations in phytoplankton

483    production at DYFAMED time-series station, northwestern Mediterranean Sea. Deep

484    Sea Res. Part II 49, 2017–2030, 2002.

Mehrbach, C., C. H. Culberson, J. E. Hawley, and R. M. Pytkowicx .: Measurement of the apparent dissociation constants of carbonic acid in seawater at atmospheric pressure, Limnol Oceanogr, 18(6), 897-907, 1973.

Merlivat, L., and Brault, P.: CARIOCA BUOY, Carbon Dioxide Monitor, Sea Technol., 23–30, 1995.

Merlivat, L., Boutin, J., & Antoine, D. : Roles of biological and physical processes in driving seasonal air–sea CO 2 flux in the Southern Ocean: New insights from CARIOCA pCO 2. Journal of Marine Systems, 147, 9-20, 2015.

Merlivat, L., Boutin, J., Antoine, D., Beaumont, L., Golbol, M., & Vellucci, V. : Increase of dissolved inorganic carbon and decrease of pH in near surface waters of the Mediterranean Sea during the past two decades. Biogeosciences, 15(18), 5653-5662, 2018.

Millot: Circulation in the Western Mediterranean Sea, Journal of Marine Systems, 20, 423–442, 1999.

Morel, A., and J. F. Berthon . : Surface pigments, algal biomass profiles, and potential production of the euphotic layer: relationships reinvestigated in review of remote-sensing applications, Limnol. Oceanogr., 34, 1545–1562, 1989.

Niewiadomska, Katarzyna, Claustre, Hervé, Prieur, Louis, d'Ortenzio, Fabrizio, (2008), Submesoscale physical‐biogeochemical coupling across the Ligurian current (northwestern Mediterranean) using a bio‐optical glider, Limnology and Oceanography, 53, doi: 10.4319/lo.2008.53.5_part_2.2210.

Papaioannou, G., Papanikolaou, N., and Retalis, D. : Relationships of photosynthetically active radiation and shortwave irradiance. Theoretical and Applied Climatology, 48: 23–27, 1993.

Pasqueron de Fommervault, O., Migon, C., D'Ortenzio, F., Ribera d'Alcalà, M., and Coppola, L.: Temporal variability of nutrient concentrations in the northwestern Mediterranean sea (DYFAMED time-series station), Deep-Sea Res. Pt. I, 100, 1–12, 2015.

Pellichero, V., Boutin, J., Claustre, H., Merlivat, L., Sallée, J.-B., & Blain, S. : Relaxation of wind stress drives the abrupt onset of biological carbon uptake in the Kerguelen bloom: a multisensor approach. Geophysical Research Letters, 47, e2019GL085992

514 https://doi.org/10.1029/2019GL085992, 2020.

515 Rödenbeck, C., Keeling, R. F., Bakker, D. C. E., Metzl, N., Olsen, A., Sabine, C., and
516 Heimann, M.: Global surface-ocean pCO2 and sea–air CO2 flux variability from an
517 observation- driven ocean mixed-layer scheme, Ocean Sci., 9, 193–216, doi:10.5194/os-9-
518 193-2013, 2013.

519 Rumyantseva, A, Henson, S, Martin,A , Thompson, A. F, Damerell G.M, Kaiser J, Heywood,
520 K.J.: Phytoplankton spring bloom initiation: The impact of atmospheric forcing and light in
521 the temperate North Atlantic Ocean, Progress in Oceanography, 2019.

522 Siegel, D. A., S. C. Doney, and J. A. Yoder (2002), The North Atlantic spring phytoplankton
523 bloom and Sverdrup's critical depth hypothesis, Science, 296, 730– 733.

524 Sverdrup, H. U.: On vernal blooming of phytoplankton. Conseil Exp. Mer, 18, 287-295,1953.

525 Takahashi, T., Sutherland, S. C., Wanninkhof, R., Sweeney, C., Feely, R. A., Chipman, D. W.,
526 Hales, B., Friederich, G., Chavez, F., Sabine, C., Watson, A., Bakker, D. C. E., Schuster, U.,
527 Metzl, N., Yoshikawa-Inoue, H., Ishii, M., Midorikawa, T., Nojiri, Y., Kortzinger, A.,
528 Steinhoff, T., Hoppema, M., Olafsson, J., Arnarson, T. S., Tillbrook, B., Johannessen, T.and
529 Olsen, A., Bellerby, R., Wong, C. S., Delille, B., Bates, N. R., and de Baar, H. J. W.:
530 Climatological mean and decadal change in surface ocean pCO2 and net sea-air CO2 flux
531 over the global oceans, Deep-Sea Res. II, 56, 554–577, 2009.

532 Taylor, J. R., & Ferrari, R.: Shutdown of turbulent convection as a new criterion for the onset

533 of spring phytoplankton blooms. Limnology and Oceanography, 56(6), 2293-2307, 2011.

534 Venables, H. and Moore, C.M.: Phytoplankton and light limitation in the Southern Ocean:
535 Learning from high nutrient, high chlorophyll areas. Journal of Geophysical Research:
536 Oceans, 115(C2), 2010.

537 Wanninkhof, R.: Relationship between wind speed and gas exchange over the ocean revisited.
538 Limnology and Oceanography: Methods, 12(6), 351–362, 2014.

539 Weiss, R.: Carbon dioxide in water and seawater: the solubility of a non-ideal gas, Marine
540 chemistry , 2 (3), 203–215, 1974

541

543    Figures and tables

544    Figure 1. The area of the northwestern Mediterranean Sea showing the French and Italian
545    Rivieras, the island of Corsica, the main current branches (green arrows) in the Ligurian Sea
546    and the location of the BOUSSOLE buoy (white square) and the AZUR meteorological buoy
547    (yellow square). The black line indicates the glider's path in March-April 2016.

548    Figure 2. 2016 (a) Hourly DIC (green) and SST (purple) at the BOUSSOLE site, (b) hourly
549    wind stress (blue) and net heat flux (pink) at the Azur buoy site. The pink dotted line indicates
550    the change of sign of the net heat flux from negative to positive values,  (c) daily depths of the
551    mixed layer (black), mixing layer (dotted black), Ekman layer (cyan) and euphotic layer
552    (orange) at the BOUSSOLE site. The black dotted line on panels (a), (b), (c) (d) and (e)
553    indicates the onset time of the bloom (18 March). (d) PAR (orange) and average mixing layer
554    irradiance (blue), (e) Glider-derived depths of the mixed layer (black curve, same as in (c)),
555    euphotic layer (orange), and nighttime 2-day binned chlorophyll concentration (green
556    coloring) retrieved between March 7 and April 5.

557    Figure 3. (a, b, c) 2017, 2018 and 2019 DIC (green) and SST (purple) at the BOUSSOLE site,
558    (d, e, f) wind stress (blue) and net heat flux (red) at the Azur buoy site. The red dotted line
559    indicates the change of sign of the net heat flux from negative to positive values, (g, h, i)
560    depths of the mixing layer (dotted black), Ekman layer (cyan) and euphotic layer (orange) at
561    the BOUSSOLE site. The vertical dotted green line indicates the onset of the bloom.

562    Figure 4. Changes of physical parameters (hourly values) at the onset of the 2016 bloom
563    during 2 consecutive periods of 4 days, March 14-17 (blue) and March 18-21 (red) as a
564    function of wind stress (a) net surface heat flux (b) depths of the Ekman, mixing and euphotic
565    layer. Grey circles and grey squares indicate mean values respectively on March 17 and
566    March 18. For comparison, the orange line shows the euphotic layer depth (March 14-21).

567    Figure 5. From March 7 to April 5, (a) DIC and Chla. The purple line and the squares
568    (blue,morning; grey, evening) indicate the 3 days biological diurnal DIC changes during the
569    period considered to compute NCP The blue and orange lines indicate the surface Chla when
570    the glider was at a distance of less than 5 km (blue) and less than 20 km (orange) respectively
571    from the BOUSSOLE buoy. (b) PAR and I average mixing layer irradiance. The vertical
572    dotted black line indicates the onset of the bloom on March 18.

573 Table 1. Net community production computed in the mixing layer over 3 days (NCP) after the
574 bloom onset ($T_0$). (a, b) variation of DIC at the measurement depth and linked correlation
575 coefficient; (c, d) change of integrated DIC over $Z_{mx}$ and linked correlation coefficient ;(e)
576 $CO_2$ flux from the atmosphere to the ocean; (f), absolute value of calculated NCP is
577 considered in order to provide positive values throughout the presentation and discussion in
578 the manuscript.

579 Table 2. 2016-2019. Atmospheric drivers of the onset of the bloom: average values and
580 standard deviation on the day of the start of the bloom, $T_0$.

581